nature communications

Article

https://doi.org/10.1038/s41467-025-65127-x

Reduced aerosol pollution diminished cloud reflectivity over the North Atlantic and Northeast Pacific

Received: 6 May 2025

Accepted: 8 October 2025

Published online: 05 November 2025

Check for updates

Knut von Salzen[1,2] ✉, Ayodeji Akingunola[2], Jason N. S. Cole[2], Ruth A. R. Digby[2], Sarah J. Doherty[3], Luke Fraser-Leach[4], Edward Gryspeerdt[5], Michael Sigmond[2] & Robert Wood[1]

Over the past several decades, the proportion of solar radiation reflected back into space has declined, accelerating the accumulation of heat within the Earth system. Here we show that the marine cloud reflectivity decreased on average by 2.8 ± 1.2% per decade in the combined North Atlantic and Northeast Pacific regions between 2003 and 2022. The majority of the Earth System Models we analyzed simulated a significantly weaker cloud reflectivity decrease and warming of the sea surface in these regions than observed. In contrast, our simulations using an improved aerosol-climate model reproduce the spatial extent and magnitude of the observed cloud reflectivity decrease. We show that reductions in sulfur dioxide and other aerosol precursors accounted for 69% (range 55–85%) of the cloud reflectivity decrease through aerosol-cloud interactions, consistent with the observed aerosol and cloud trends. This raises the prospect of a continuing cloud reflectivity decrease and an associated warming impact in these regions, given that the emission reductions are projected to persist over the next few decades. Further research is needed to assess whether near-term climate scenarios should be revised to account for the weak cloud reflectivity reductions in the Earth System Models.

Recent studies have warned of an unexplained warming surge, with new global temperature records set in both 2023 and 2024[1–8]. These temperature extremes were preceded by a multi-decadal decline in the proportion of solar radiation reflected back into space by low-level clouds, leading to an increasing amount of shortwave radiation reaching the ocean, with this trend accelerating in recent years[7,9–13]. The reductions in low-level cloud reflectivity reached a new extreme in the extratropical Northern Hemisphere in 2023 and 2024[14].

Regionally, North Atlantic sea surface temperatures (SSTs) have been rising faster than elsewhere[12,14]. In the Northeast Pacific, a period of persistent marine heatwaves beginning in 2014 has had devastating impacts on marine ecosystems and fisheries[15,16]. The exceptional sea surface temperatures cannot be explained by the historically observed Pacific Decadal Oscillation, which had been the dominant mode of long-term SST variability prior to 2014[17,18].

It is currently unknown whether the multi-decadal decline in cloud reflectivity has increased the likelihood of the temperature records in 2023 and 2024. This seems probable given that the time for the climate system to respond to a perturbation in radiative fluxes is measured in years to decades[19,20]. Overall, the causes of the recent rapid warming, and the cloud reflectivity reduction possibly driving it, remain poorly understood. Volcanic eruptions, variations in solar

[1]Department of Atmospheric and Climate Science, University of Washington, 408 Atmospheric Sciences-Geophysics (ATG) Building Box 351640, Seattle 98195 WA, USA. [2]Canadian Centre for Climate Modelling and Analysis, Environment and Climate Change Canada, 2474 Arbutus Road, Victoria V8N 1V8 BC, Canada. [3]Cooperative Institute of Climate, Ocean and Ecosystem Studies, University of Washington, John M. Wallace Hall, 3737 Brooklyn Ave NE, Seattle 98105 WA, USA. [4]Department of Physics, University of Toronto, 60 St George St, Toronto M5S 1A7 ON, Canada. [5]Department of Physics, Imperial College London, 708, Huxley Building, South Kensington Campus, London SW7 2BX, UK. ✉e-mail: kvsalzen@uw.edu

activity, and the El Niño Southern Oscillation are unlikely to have notably contributed[14,21,22]. Simulations conducted with different Earth System Model (ESM) ensembles have largely failed to replicate the full magnitude of the observed changes[5,7,11,21]. The daunting possibility exists that the current predictive capabilities are underestimating the warming of the Earth system[21–23]. In addition to a possible underestimation in shortwave cloud feedbacks[24], various studies have emphasized the need for better understanding of the role of aerosol changes on cloud reflectivity trends. Globally, emissions of aerosols and precursors have been declining for more than a decade, primarily due to the introduction of stricter standards for sulfur dioxide (SO_2) in China[25–27] and other countries in the Northern Hemisphere, consistent with earlier analyses of satellite observations[28,29]. Given that aerosols can form cloud droplets by serving as cloud condensation nuclei, reductions in aerosols have resulted in decreased cloud droplet concentrations in regions affected by declining emissions[29]. This could have reduced the cloud reflectivity[30,31], but the extent of the climate impacts of these changes remains uncertain[21,23]. Complicating the matter, the chemical composition of the aerosols and therefore their impacts on climate can vary, depending on the source of the emissions[32,33]. Most significantly, assessments of the role of aerosols in the observed trends are affected by known biases and large uncertainties in simulated aerosol-cloud interactions in the current generation of ESMs[34].

Here we first establish whether the rapidly declining cloud reflectivity in the North Atlantic and Northeast Pacific correlates with aerosol reductions in satellite observations and Earth Systen Model simulations. We then used a newly developed version of the global Canadian Atmospheric Model (CanAM5.1-PAM) to determine the contributions of aerosol reductions and SST changes to the observed aerosol and cloud trends. Finally, we analyzed the model simulations to determine the contributions of key aerosol-cloud interactions to the observed trends.

Results

Observed cloud trends

Our analysis of two decades of satellite observations from the Clouds and the Earth's Radiant Energy System (CERES) Energy Balanced and Filled (EBAF) Ed4.2 dataset[35–37] show that clouds have become considerably less reflective over the combined North Atlantic and Northeast Pacific regions over the recent 20-year long period from January 1, 2003 to December 31, 2022, consistent with earlier studies[7,13,14]. In these regions, the shortwave cloud radiative effect (CRE), which is the difference between the solar radiation that would be reflected back to space without clouds and the actual reflected radiation, weakened more rapidly than anywhere else in the Northern Hemisphere (Figs. 1, S1). Over these 2 decades, the annual mean CRE over the North Atlantic and Northeast Pacific steadily increased to less negative values by 0.91 ± 0.64 W m^{-2} decade^{-1} (95% confidence) and 1.18 ± 0.86 W m^{-2} decade^{-1}, respectively. The mean trend for the combined North Atlantic and Northeast Pacific regions was 1.04 ± 0.45 W m^{-2} decade^{-1}, a relative change of $2.8 \pm 1.2\%$ decade^{-1}. This implies a contribution to the Earth's global energy budget of 0.15 ± 0.06 W m^{-2} decade^{-1}, given that these marine regions cover 14% of the Earth's surface area.

Consistent with ref. 13 and ref. 14 we find that the CRE increase was by far the leading cause of the observed reduction in total reflected solar radiation (Figs. S2 and S3). Given the surface warming, a moderate increase in outgoing longwave radiation was observed, which acted to dampen the warming trend (ref. 14, Figs. S2 and S3). Furthermore, the CRE increase was associated with a reduction in total cloud fraction and increase in cloud droplet size (Figs. S2 and S3). Our simulations show that changes in cloud fraction and droplets both contributed to the observed CRE trend (Drivers of cloud trends).

Over the same time period, the observed SST in the HadCRUT5 dataset[38,39] increased significantly over large regions of the ocean, with a particularly rapid warming of 0.19 ± 0.08 K decade^{-1} in the North Atlantic and Northeast Pacific, in close proximity to the observed extrema in the CRE and cloud fraction trends (Figs. 1, S1, and S2). These changes can be partly explained by the marine low cloud feedback, which can be expected to amplify the observed warming in these regions[24]. The fraction and reflectivity of clouds are known to be impacted by various meteorological controlling factors. ref. 40 concluded that a decrease in the strength of the temperature inversion and an SST increase caused the low cloud fraction to decrease in the Northeast Pacific region between 2001 and 2020. Similar, ref. 41 attributed reductions in cloud fraction and reflected shortwave radiation over the North Atlantic between 1970 and 2014 to greenhouse gas-induced warming. However, the extent to which cloud-controlling factors influenced the regional CRE trends remains uncertain.

Similar to ref. 42, we find that the observed CRE and SST trends cannot be solely attributed to the unforced internal climate variability in the trends in these regions, which we estimate to be within the ranges of ± 0.38 W m^{-2} decade^{-1} for the CRE and ± 0.11 K decade^{-1} for the SST (Methods). Therefore, a key question is whether the observed clouds trends were ultimately forced by changing fossil fuel and biofuel sources of aerosols. Indeed, we find evidence for rapidly changing cloud processes that are indicative of aerosol impacts on cloud reflectivity. Many cloud processes depend on the cloud droplet number concentration (N_d), including precipitation efficiency and cloud optical properties. Satellite observations of N_d using data from the Moderate Resolution Imaging Spectroradiometer (MODIS) Terra instruments (Methods) provide evidence for notable reductions in N_d over the North Atlantic (-6.7 ± 1.5 cm^{-3} decade^{-1}) and Northeast Pacific (-2.9 ± 1.7 cm^{-3} decade^{-1}). The co-location and magnitudes of the N_d and CRE trends raises the question whether aerosol reductions may have contributed to the CRE increase. Cloud droplets form as water vapor condenses on aerosol particles that are sufficiently large and water-soluble, widely referred to as cloud condensation nuclei. Both observations and models show that marine boundary layer cloud reflectivity is increased as the concentration of aerosols from emissions of SO_2 increases[43]. Further, the reflectivity of the persistent region of boundary-layer clouds over the Northeast Pacific has been shown to be particularly susceptible to changes in aerosol concentrations[44].

The importance of aerosol-cloud interactions for the CRE trends is further supported by the high correlation between the N_d trends and reductions in aerosol optical depth (AOD) over the North Atlantic (-0.0063 ± 0.0035 decade^{-1}) and Northeast Pacific (-0.0069 ± 0.0035 decade^{-1}), as derived from the Multiangle Imaging SpectroRadiometer (MISR) Level 3 Global Joint Aerosol monthly product V002 (refs. 45–47, Figs. 1 and S1). The pronounced reductions in AOD along the eastern boundaries of Eurasia and North America indicate that these were caused by declining anthropogenic emissions of SO_2 and other aerosol precursors over large regions of these continents. Annual anthropogenic emissions of SO_2 from China and the United States of America declined rapidly over the 20 year period of the observational data (-15.9 and -7.1 Mt decade^{-1}, respectively, Figs. S4 and S5), largely owing to the introduction of stringent standards for emissions from power plants aimed at improving air quality in these countries[25,48–51].

Earth System Model Simulations

To analyze the causes of the observed CRE increase we first turned to results from 24 ESMs that participated in the Coupled Model Intercomparison Project Phase 6 (CMIP6[52], Supplementary Table 1). These models provide the radiative fluxes required for the calculation of the CRE, using the future SSP2-4.5 scenario[11] between January 1, 2015 and December 31, 2022 (Methods).

We find that the both the spatial extent and magnitude of the CMIP6 multi-model mean simulated CRE increase are weaker than

https://doi.org/10.1038/s41467-025-65127-x

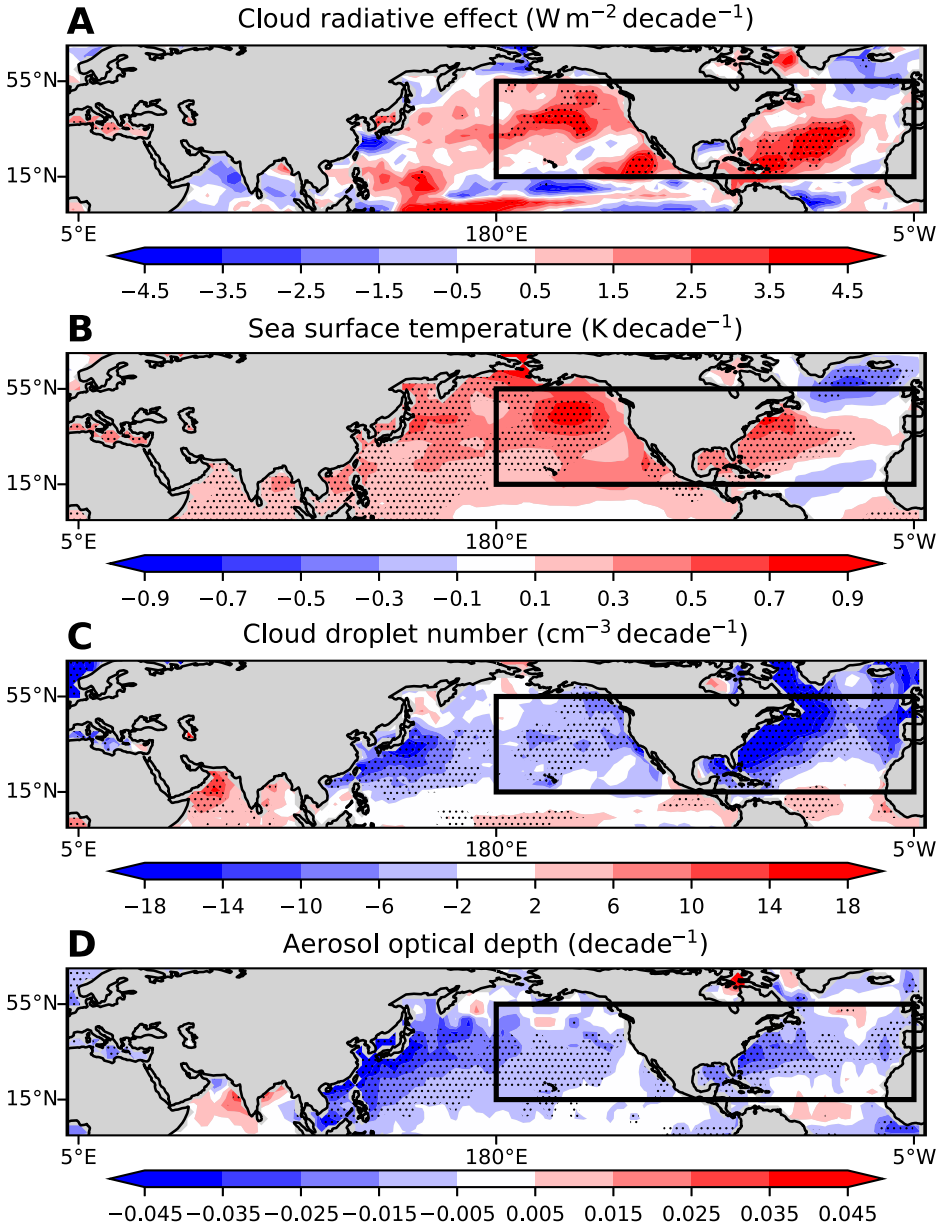

Fig. 1 | Observed changes in clouds, sea surface temperature, and aerosols. The linear trends in annual mean shortwave cloud radiative effect (CRE, **A**), sea surface temperature (SST, **B**), cloud droplet number concentration at cloud top (N_d, **C**), and aerosol optical depth at 550 nm (**D**), from January 1, 2003 to December 31, 2022. Stippling indicates that the trends are statistically significant (95% confidence interval). The corresponding annual averages for the Northeast Pacific and North Atlantic regions, bounded by 180°E to 5°W and 15°N to 55°N (black rectangle), are shown in Fig. S1. Here and elsewhere, averages refer to the marine regions within these boundaries. See "Methods" for details.

observed (Fig. 2A). According to the CERES satellite observations, the CRE experienced an increase in 80% of the combined North Atlantic and Northeast Pacific regions, whereas the simulated CRE increased in 64% of these regions within the multi-model ensemble (ranging from 45 to 86%). The CRE trend surpassed 2 W m^{-2} decade^{-1} in 21% (ranging from 5 to 46%) of the regions within the multi-model ensemble, which is considerably less than the observed 34%.

Similarly, the multi-model mean underestimates the extensive spatial extent and the intensity of the observed SST warming, exhibiting a comparable pattern to the CRE trends (Fig. S6). Consequently, the CMIP6 multi-model mean CRE and surface temperature trends in these regions are weaker than observed, with simulated CRE and temperature trends of 0.42 W m^{-2} decade^{-1} (range from -0.2 to 1.15 W m^{-2} decade^{-1}) and 0.15 K decade^{-1} (range from 0 to 0.42 K decade^{-1}), respectively. In comparison, the observed trends are 1.04 ± 0.45 W m^{-2} decade^{-1} and 0.19 ± 0.08 K decade^{-1} (Fig. 3), respectively.

Despite the differences in simulated SST and CRE trends, observations and models consistently indicate that the warming was more pronounced in areas with rapidly increasing CRE (Fig. 2B). The simulated and observed relationships between CRE and SST trends exhibit surprisingly similar patterns across many models, despite significant differences in the trends. The reasons for the similarity in these patterns remain unclear. ref. 53 found SST variations in phase with solar activity across the Indian, Pacific, and Atlantic oceans. By analyzing the relationship between these variations they were able to derive an ocean climate sensitivity to changing solar irradiance at the top of the atmosphere of 0.08 K W^{-1} m^2 on decadal and 0.14 K W^{-1} m^2 on interdecadal time scales, the same order as the simulated changes in Fig. 2B.

https://doi.org/10.1038/s41467-025-65127-x

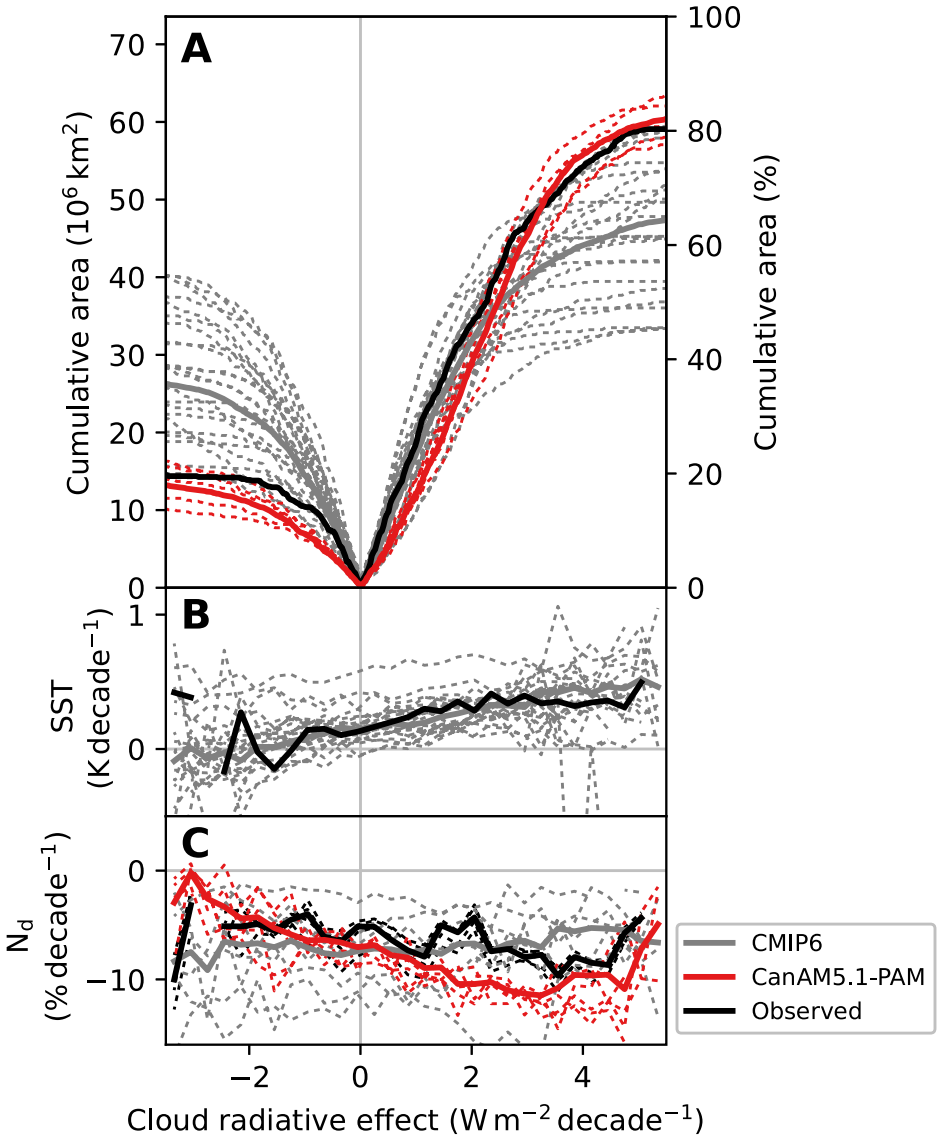

Fig. 2 | The spatial extents and magnitudes of the trends. Cumulative area within the North Atlantic plus Northeast Pacific regions (Fig. 1) for which the decadal trend of the cloud radiative effect (CRE) falls between nil and the value indicated on the abscissa (**A**). The trends of the sea surface temperature (SST, **B**) and cloud droplet number concentration (N_d, **C**) in these locations are also shown. The black line corresponds to the observational data sets as described in "Observed cloud trends". The gray lines refer to results from simulations with 24 Coupled Model Intercomparison Project Phase 6 (CMIP6) Earth System Models, which includes a subset of models that provided N_d. Results from simulations with the model CanAM5.1-PAM are shown in red, which incorporates the Twomey and Albrecht effects (Earth System Model simulations). Thick lines refer to ensemble mean results and dashed lines to the individual ensemble members. See "Observed cloud trends", "Earth System Model simulations", and the Supplementary Notes for details.

To understand the differences in the CMIP6 multi-model ensemble simulations, we separated the models into two groups. Ten of the CMIP6 models simulate CRE trends that are not significantly different from the observed CRE trend (95% confidence), with a mean simulated CRE trend of 0.84 W m^{-2} decade^{-1} (range from 0.15 to 1.15 W m^{-2} decade^{-1}). The mean SST trend simulated by these models (0.20 K decade^{-1}, range from 0.03 to 0.34 K decade^{-1}) agrees well with the observed SST trend. Given the good agreement of the simulated and observed CRE and SST trends we refer to these as the "best" models. Cloud droplet number concentrations are available for 4 of these 10 models, which we used to calculate a multi-model mean trend of -4.45 cm^{-3} decade^{-1} (range from −9.53 to -0.73 cm^{-3} decade^{-1}), which also agrees well with the observations (-4.86 ± 1.32 cm^{-3} decade^{-1}).

In contrast, the remaining 14 models simulate CRE trends that are significantly weaker than the observed CRE trend, with a mean simulated trend of 0.12 W m^{-2} decade^{-1} (range from -0.20 to 0.38 W m^{-2} decade^{-1}). None of these "other" models simulate trends exceeding the observed trend. Furthermore, the mean temperature trend tends to be lower than for the "best" models (0.12 K decade^{-1}, range from 0 to 0.42 K decade^{-1}). The mean N_d trend in the three models that provide N_d data also tends to be considerably weaker than observed (-2.02 cm^{-3} decade^{-1}, range from -5.13 to -0.31 cm^{-3} decade^{-1}).

While the results from the "best" and "other" models appear to be consistent with our expectation that the CRE and SST should increase more rapidly in models that simulate strong reductions in N_d, we were unable to robustly determine the extent to which biases in simulated N_d and aerosol-cloud interactions contribute to the weak CRE and surface temperature trends in the CMIP6 multi-model ensemble because there are not sufficient data available for N_d.

Drivers of cloud trends

To assess the impacts of aerosols and cloud microphysical processes on CRE trends we conducted additional simulations with CanAM5.1-PAM, which combines the established climate modeling capabilities

https://doi.org/10.1038/s41467-025-65127-x

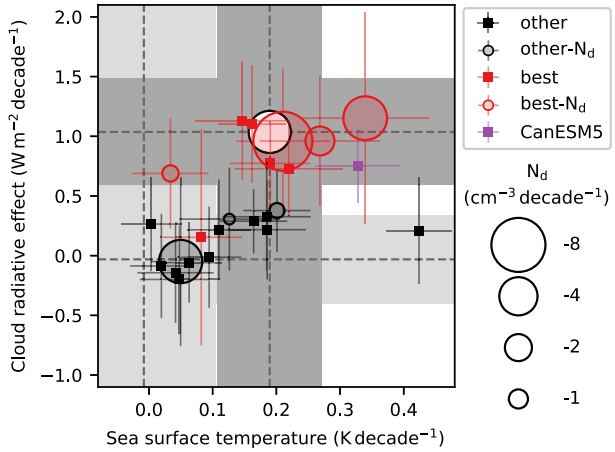

Fig. 3 | Regionally averaged trends in Earth System Models and observations. The mean trends in cloud radiative effect (CRE), sea surface temperature (SST), and cloud droplet number concentration (N_d) in the North Atlantic and Northeast Pacific regions in the observations (white circle) and in the simulations with the Coupled Model Intercomparison Project Phase 6 (CMIP6) Earth System Models. Where available, the magnitude of the trends in N_d is indicated by the size of the circles. Otherwise, where N_d is not available, squares are used. The CMIP6 models are grouped into "best" (red and purple) and "other" (black) models, as described in the text. The purple square refers to results from the CanESM5 model. 95% confidence intervals are shown for the observed trends (dark gray shading), the ranges associated with internal unforced climate variability (lighter gray shading), and the model ensemble member trends (gray, red, and purple whiskers).

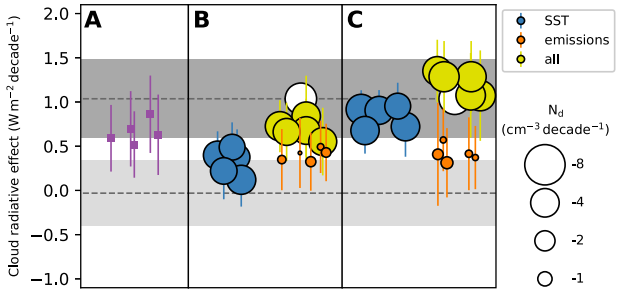

Fig. 4 | The factors influencing cloud trends in the CanAM5.1-PAM model. The mean trends in cloud radiative effect (CRE) and cloud droplet number concentration (N_d) in the North Atlantic and Northeast Pacific regions in the observations (white circle) and in three atmospheric global climate model ensembles with specified sea surface temperature (SST): Simulations of the Twomey effect in the models CanAM5.1 (**A**), CanAM5.1-PAM (**B**), and the combined Twomey and Albrecht effects in CanAM5.1-PAM (**C**). For (**B**, **C**) simulations using specified SSTs from 2003 to 2022 (yellow) are compared to simulations with specified perpetual SSTs from year 2000 (blue) and with specified perpetual emissions from year 2000 (orange). 95% confidence intervals are shown for the observed trends (dark gray shading), the ranges associated with internal unforced climate variability (lighter gray shading), and the model ensemble member trends (whiskers). The magnitude of the trend in N_d is indicated by the size of the circles.

for the global atmosphere in CanAM5.1[54,55] with new and improved modeling capabilities for aerosol-cloud interactions. In particular, it includes an advanced numerical representation of the aerosol size distribution[56] and of the formation of cloud droplets through aerosol activation[57]. Only minor differences exist between CanAM5.1 and the earlier model version CanAM5[54] in the Earth System Model CanESM5 (ref. 58, Methods).

Results from CanAM5.1-PAM for aerosols agree well with in-situ observations from field campaigns and long-term monitoring[56,57,59], with a simulated aerosol radiative forcing within previously assessed ranges (Methods). By specifying the SSTs in CanAM5.1-PAM, following the CMIP6 protocol, it is possible to robustly distinguish and compare the impacts of SSTs and aerosols on the regional cloud trends.

Different configurations of CanAM5.1-PAM are available that allowed us to attribute trends in simulated CRE trends to two key processes. First, decreasing anthropogenic aerosol emissions can lead to lower cloud reflectivity via the Twomey effect. In particular, a decrease in N_d results in larger cloud droplets if the cloud liquid water content does not change, which reduces the cloud albedo[30]. Second, if the cloud is precipitating, the cloud liquid water content may decrease as aerosol concentrations decrease. This is because larger droplets take less time to coalesce into raindrop size, enhancing precipitation efficiency. Consequently, the lifetime of the cloud is reduced, which reduces the reflectivity further, beyond the Twomey effect. This is commonly referred to as the Albrecht effect[31].

We used CanAM5.1-PAM with specified SSTs to conduct two distinct sets of simulations. One set incorporates only the Twomey effect, while the other set encompasses both the Twomey and Albrecht effects (Methods). In the CanAM5.1-PAM simulations in which aerosol-cloud interactions are governed only by the Twomey effect, the CRE increases in 73% (range 70–74%) of the combined North Atlantic and Northeast Pacific regions (Figs. S7–S10), which is less than observed. With the addition of the Albrecht effect in CanAM5.1-PAM, the CRE increases in 82% of the regions (range 78–86%, Figs. 2 and S11–S14), in good agreement with the observations (Observed cloud trends). The mean simulated CRE trend of 1.21 W m^{-2} decade^{-1} (range from 1.07 to 1.35 W m^{-2} decade^{-1}) is statistically indistinguishable from the observed trend (Fig. 4B) and agrees well with the mean trend simulated by the 10 "best" CMIP6 models. Similar to the observations and results from the "best" CMIP6 models, the CRE increase is associated with a notable decrease in N_d of -4.37 cm^{-3} decade^{-1} (range from -4.54 to -4.11 cm^{-3} decade^{-1}). Wide-spread reductions of 5–10% are simulated, with the most rapid losses occurring for CRE trends greater than -2 W m^{-2}, similar to the observations.

In the simulation with the Albrecht effect the loss of cloud fraction nearly doubles to −3.2% decade^{-1} (range -4.2 to − 2.0 decade^{-1}) from −1.7 decade^{-1} (range -2.9 to −0.5 decade^{-1}) in the simulation with the Twomey effect. The former is similar to the observed trend of −4.2 ± 0.3 decade^{-1}.

To determine the contribution of the SST changes to the CRE trends, we compared the CRE trends to results from simulations with perpetual monthly anthropogenic emissions from the year 2000 instead of the time-varying emissions. This produced aerosol and cloud droplet concentrations that remained nearly constant (Fig. 4). Although the CRE also increases in these simulations, the probability that the simulated CRE increase falls within the standard error of the observations (0.23 W m^{-2} decade^{-1}) is only 5% (Supplementary Notes), which indicates that the SST increase is unlikely to be the sole cause of the observed CRE increase.

Based on our simulations with the different configurations of CanAM5.1-PAM we find that 0.80 W m^{-2} decade^{-1} (range 0.5 to 1.0 W m^{-2} decade^{-1}), or 69% (range 55–85%) of the total simulated CRE increase can be explained by the impact of the declining emissions on the combined Twomey and Albrecht effects. Individually, the Twomey and Albrecht effects contributed 0.29W m^{-2} decade^{-1} (range 0.1 to 0.5 W m^{-2} decade^{-1}) and 0.51 W m^{-2} decade^{-1} (range 0.15 to 0.85 W m^{-2} decade^{-1}), respectively (Fig. 5). In comparison, the SST changes since 2000 contributed 0.38 W m^{-2} decade^{-1} (range 0.12 to 0.65 W m^{-2} decade^{-1}), or 31% (range 15–45%). The latter may be overestimated, given that cloud feedbacks in this model are generally stronger than in many other ESMs[60–62].

Discussion

Our analysis of the observed cloud trends in the combined North Atlantic and Northeast Pacific regions from 2003 to 2022 is consistent with the scientifically widely accepted view that atmospheric aerosols

https://doi.org/10.1038/s41467-025-65127-x

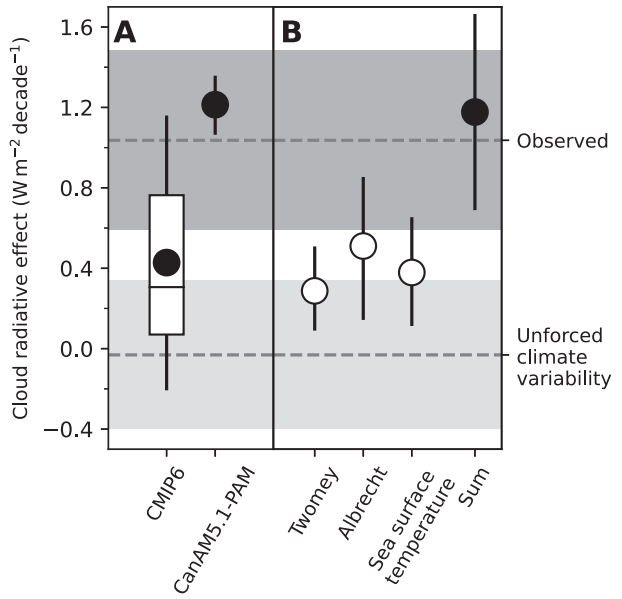

Fig. 5 | Summary of the key processes driving the cloud trends. The linear cloud radiative effect (CRE) trends and the factors that were driving them in the combined North Atlantic and Northeast Pacific regions. The gray shading refers to the 95% confidence intervals of the observed trend (dark gray) and the internal unforced climate variability (light gray). In (**A**), the trends simulated by the Coupled Model Intercomparison Project Phase 6 (CMIP6) multi-model ensemble are displayed on the far left. The box extends from the first to the third quartile and whiskers from the minimum to the maximum simulated 20 year mean CRE trend. The median and mean CMIP6 trends are indicated by the horizontal line and the black bullet, respectively. The CMIP6 results are compared to our simulations of the combined Twomey and Albrecht effects in the CanAM5.1-PAM model. In (**B**), the latter is broken down into the separate contributions associated with the Twomey and Albrecht effects and the sea surface temperature trend. See "Earth System Model simulations" and "Methods" for details.

from fossil fuel and biofuel combustion sources have historically masked some of the warming effect that results from the emissions of greenhouse gases[9,33,63,64]. After sulfur dioxide emissions peaked sometime in the early 2000's[65], and with that aerosol impacts on clouds and climate, the extent to which the greenhouse gas-induced warming is being masked by aerosols has lessened. Specifically, the aerosol reductions resulted in a decrease in cloud droplet number concentration, consequently decreasing cloud reflectivity. Both the Twomey and Albrecht effects contributed to this cloud reflectivity decrease. This increased the absorption of solar radiation by the ocean and caused an acceleration in the warming of the surface ocean. These changes are significant over the North Atlantic and Northeast Pacific where aerosols have been rapidly declining.

In addition to increasing the absorption of solar radiation, the decrease in cloud reflectivity likely contributed to the warming of the sea surface through cloud feedbacks, which enhanced the loss of cloud reflectivity further as these regions were warming[24]. However, we found that the warming-induced loss of cloud reflectivity, from the aerosol and greenhouse gas changes, was less impactful than the decrease in cloud droplet number.

Our analysis shows that reductions in emissions of sulfur dioxide and other aerosol precursors were responsible for a significant fraction of the recent radiative forcing changes in these regions. For example, CO_2 concentrations at the Mauna Loa observatory increased by 22.7 ppm decade^{-1} from January 1, 2003 to December 31, 2022. This corresponds to an increase in the global CO_2 radiative forcing at the top of the atmosphere of 0.31 W m^{-2} decade^{-1} (Methods). In comparison, over the same period, the cloud radiative effect in the combined North Atlantic and Northeast Pacific regions increased by 1.04 ± 0.45 W m^{-2} decade^{-1}. This likely resulted in a disproportionate warming impact, considering the spatial inhomogeneity of the radiative forcing changes[66]. However, it is unclear how the recent radiative forcing and temperature changes in these regions compare to those observed in other regions and how changes in different regions are related.

Furthermore, the cloud reflectivity reduction exceeded the reduction in clear-sky atmospheric reflectivity in these regions, which is consistent with our model simulations. In comparison, the analysis by ref. 67 indicates that the reduction in global reflection of shortwave radiation to space between 2000 and 2020 was caused almost equally by reductions in cloudy and clear-sky atmospheric scattering. It would be beneficial for future research to assess aerosol impacts on clouds and clear-sky scattering in other regions, and globally.

The shared socio-economic pathway scenarios used by the Intergovernmental Panel on Climate Change and a range of clean air policy scenarios project that the aerosol concentrations and the number of cloud droplets will continue to decline over the next few decades in the combined North Atlantic and Northeast Pacific regions[23,33,65]. Given the fundamentally non-linear nature of aerosol-cloud interactions, even relatively minor additional reductions in cloud droplet number could decrease cloud reflectivity notably as the air becomes increasingly clean. The expected continuation of emission reductions may therefore play a significant role in affecting near-term climate trends in these regions, adding to the warming produced by the aerosol emission reductions to date. However, the extent to which climate projections beyond 2022 could be affected by aerosol emission-driven cloud reflectivity changes is currently unknown.

The recent cloud changes are an unintended consequence of efforts to improve air quality and reduce health risks[68]. Our analysis based on different versions of the global Canadian Atmospheric Model (CanAM) draws attention to the need to better account for aerosol-cloud interactions in the global Earth System Models, many of which have been found to underestimate the observed cloud reflectivity reductions in simulations driven by historical and scenario emissions. This limits the capacity to accurately assess near-term changes in the sea surface temperature based on projections with these models. A comprehensive understanding of recent changes in aerosols and clouds, and modeling capabilities to simulate these, is therefore essential to inform climate mitigation and adaptation decisions.

Methods

Observations

The CERES instruments on the Terra and Aqua platforms separately measure filtered radiances in the shortwave between 0.3 and 5 µm, total between 0.3 and 200 µm, and window region between 8 and 12 μm wavelengths. The filtered radiances are converted to unfiltered radiances, which in turn are converted to instantaneous radiative fluxes at the top of the atmosphere using empirical angular distribution models[35]. The impacts of calibration uncertainties on trends are small compared to the internal unforced climate variability in radiative fluxes. ref. 69 estimated the trend uncertainty in the CRE retrievals due to instrument drift to be <0.085 W m^{-2} decade^{-1}.

Four different sampling strategies were used by ref. 70 to estimate the gridded, monthly-mean N_d from the MODIS collection 6.1 (MOD06_L2) cloud optical depth and effective radius retrievals[71]. For Figs. 1 and 2 we averaged the results of the different sampling strategies for the Terra platform available for 2.1 µm, after extending these data sets to December 2022. We also repeated the calculations using data from the MODIS Aqua platform, which produced similar trend patterns, with statistically significant reductions in the North Atlantic and Northeast Pacific regions that are of interest here (Figs. S15 and S16).

The regional patterns in AOD trends based on the MISR Level 3 Global Joint Aerosol monthly product V002 are consistent with various

other satellites and surface-based remote sensing products even though the uncertainties in AOD retrievals are substantial[28,29].

The carbon dioxide data on Mauna Loa was obtained from the NOAA Global Monitoring Laboratory[72]. The corresponding radiative forcing of CO_2 at the top of the atmosphere was calculated using the method proposed by ref. 73.

Modeling

CanAM5.1-PAM is a spectral atmospheric general circulation model that employs 49 vertical levels that extend from the surface up to 1 hPa. The spectral representation of the horizontal fields is triangularly truncated at a wave number of 63 (T63). The simulations were performed following the Atmosphere Model Intercomparison Project (AMIP) configuration employing specified boundary conditions of sea-surface temperature and sea-ice concentration. Changes in greenhouse gas abundances, land-use, volcanic aerosols, and the solar constant are also specified[52].

Aerosol chemical and microphysical processes in CanAM5.1-PAM are represented using the Piecewise-Lognormal Aerosol Model (PAM)[56,57,74], which replaces the bulk aerosol scheme and parameterization of cloud droplet number used in CanAM5.1[55]. CanAM5.1 differs from the earlier version CanAM5[54] in CanESM5[58] by using an improved representation of bulk dust aerosol concentrations. Consequently, these previous model versions differ from CanAM5.1-PAM in their representation of the Twomey effect and aerosol-radiation interactions, as distinct aerosol schemes are simulated in these models, while maintaining otherwise identical atmospheric process representations. In addition, the Albrecht effect is not included in simulations with CanAM5.1 and CanESM5. The simulated CRE trends in these models tends to be lower than observed, which aligns with the CanAM5.1-PAM simulations in which aerosol-cloud interactions are governed solely by the Twomey effect (Figs. 3, 4A).

Simulations of key climate variables and model biases are similar in CanAM5.1-PAM and CanAM5 (Figs. S18–23). Stratocumulus and cumulus regimes are well represented in the model. For instance, ref. 75 found that the simulated flux changes along the equator and Eastern Pacific during July 2000 to June 2017 in CanAM5 agree well with the observed changes, compared to other models. Simulated cloud fractions of shallow cumulus clouds in CanAM5 and CanAM4 also agree well with observations[76,77]. The structure of cloud biases in CanAM5 agrees better with observations than CanAM4 and the results are largely consistent with previous multi-model studies[54].

In addition to the Twomey and Albrecht effects simulated in CanAM5.1-PAM, larger droplets make the cloud less susceptible to evaporation with the entrainment of dry air from above the cloud. Larger droplets sediment more rapidly, so are less likely to be exposed to dry entrained air. This tends to decrease cloud evaporation and enhance cloud water content, which dampens the Twomey and Albrecht effects[78]. These and other similarly complex cloud adjustments act to modulate the Twomey effect and are not usually fully accounted for in the CMIP6 ESMs, including CanAM5.1-PAM[79]. Currently it is unknown whether the cloud adjustments could systematically enhance or reduce the CRE trends[80]. Even if cloud adjustments were fully accounted for, it is important to consider in studies of aerosol-cloud interactions that there are large differences in the magnitudes of the simulated Twomey and Albrecht effects across currently available ESMs, leading to a large range in radiative forcing through aerosol-cloud interactions, even though the importance of these processes for aerosol-cloud interactions has been well established[43,81–83].

For the simulation of the combined Twomey and Albrecht effects, the predicted N_d[57] is used to calculate the optical properties and autoconversion of cloud water to rain[84], which results in a global aerosol effective radiative forcing of -1.72 W m^2 for the combined Twomey and Albrecht effects in 2000–2014, relative to 1850, which is within the range of previous assessments[34]. The simplified version of the model that only accounts for the Twomey effect simulates a global aerosol effective radiative forcing of -1.36 W m^2. In this model version the predicted N_d is only used for the simulation of cloud optical properties and a specified constant N_d is used in the calculation of autoconversion, similar to other studies[80,85].

Emissions of SO_2, black and organic carbon from anthropogenic fossil fuel and biofuel sources in CanAM5.1-PAM are taken from the Community Emissions Data System v_2021_04_21 Release Emission Data (CEDSv2021[51,86]), with the exception of shipping emissions. The latter are from the Finnish Meteorological Institute (FMI) inventory[87], which captures the International Maritime Organization (IMO) emission regulations implemented in 2020. Biomass burning emissions for 2002–2014 were drawn from the CMIP6 historical inventory, and those for 2015–2022 were taken from the Global Fire Emissions Database (GFED v4.1s[88]).

The CEDSv2021 inventory in CanAM5.1-PAM contains lower aerosol emissions than the combined CMIP6 historical and SSP2-4.5 inventories in the CMIP6 models[89,90], due in large part to China's clean air policies, which are underestimated in the CMIP6 historical inventory before 2014[50]. However, regional linear trends in SO_2 emissions are similar in the combined inventories over the 20 years of the simulations (Fig. S5). The difference in the emissions causes negligible impacts on the simulated radiative fluxes in CanAM5.1-PAM. These are well within the uncertainty of the model ensemble simulations, according to additional simulations with the combined CMIP6 emissions (Fig. S25), similar to the conclusions by ref. 11.

N_d at cloud top in CanAM5.1-PAM is diagnosed using the simulated liquid cloud droplet radius near cloud top and cloud optical thickness according to ref. 91. The calculations supplement the Cloud Feedback Model Intercomparison Project Observational Simulator Package (COSP), which provides a collection of observation proxies that translate model-simulated cloud properties to synthetic observations that are directly comparable to satellite retrievals from CERES and MODIS.

The contributions of the Twomey and Albrecht effects and the SST changes in Fig. 5B were determined by differencing the CanAM5.1-PAM simulation results from the additional simulations with specified monthly emissions in year 2000 and SSTs, respectively.

To diagnose the unforced internal variability in the regionally averaged CRE and SST trends we used the CMIP6 preindustrial control simulation with CanESM5, wherein forcing agents are fixed at 1850 values and the model uses freely evolving lower boundary conditions. Similar to ref. 42, we diagnosed the ensemble of trends that can occur in a 20 year period, arising from internal atmospheric and oceanic variability in the model. This provided 38 consecutive trend values for each variable. We subsequently determined the unforced internal variability in the trends by multiplying the ensemble standard deviations by two[42]. We note that the results are representative of CMIP6 model results, given that the interdecadal global mean surface air temperature (GMST) variability in CanESM5 matches the CMIP6 multi-model ensemble median value of 0.07 °C[92]. Further, the unforced internal variability in globally averaged CRE trends in CanESM5 (±0.17 W m^{-2} decade^{-1}) agrees well with the estimate by ref. 42 for the CMIP6 multi-model ensemble (± 0.18 W m^{-2} decade^{-1}).

Summaries describing the CMIP6 models used here, including CanESM5, are provided in the Supplementary Table 1. Linear trends in the annual mean shortwave cloud radiative effect and sea surface temperature in these models were calculated using the monthly mean gridded data sets[52], as described in the Supplemental Notes.

Data availability

CMIP6 model data are freely available at the sites https://pcmdi.llnl.gov/CMIP6/ and https://data.ceda.ac.uk/badc/cmip6/data/CMIP6/. Observational data from CERES, MISR, MODIS, and HadCRUT are

freely available at the sites https://ceres.larc.nasa.gov/data/, https://search.earthdata.nasa.gov/, and https://www.metoffice.gov.uk/hadobs/hadcrut5/, respectively. The CanAM5 model and MODIS cloud droplet number data sets, and post-processed data used for the analysis, are available in the Zenodo database under accession code https://doi.org/10.5281/zenodo.14852523.

Code availability

The CanAM5.1 model source code and CanAM5.1-PAM updates are available at https://doi.org/10.5281/zenodo.14852522 and https://gitlab.com/PAMdev/canam5.1-pam.

References

1. Huang, B. et al. Record high sea surface temperatures in 2023. *Geophys. Res. Lett.* **51**, e2024GL108369 (2024).
2. Beaulieu, C., Gallagher, C., Killick, R., Lund, R. & Shi, X. A recent surge in global warming is not detectable yet. *Commun. Earth Environ.* **5**, 576 (2024).
3. Minobe, S. et al. Global and regional drivers for exceptional climate extremes in 2023–2024: Beyond the new normal. *Res. Square* **8**, 138 (2024).
4. Trenberth, K., Cheng, L., Pan, Y., Fasullo, J. & Mayer, M. Remarkable pattern of global warming in ocean heat content. *Res. Square* https://doi.org/10.21203/rs.3.rs-4701725/v1 (2024).
5. Tollefson, J. Earth shattered heat records in 2023 and 2024: Is global warming speeding up? *Nature* **637**, 523–524 (2025).
6. Cheng, L. et al. Record high temperatures in the ocean in 2024. *Adv. Atmos. Sci.* **42**, 1092–1109 (2025).
7. Merchant, C. J., Allan, R. P. & Embury, O. Quantifying the acceleration of multidecadal global sea surface warming driven by Earth's energy imbalance. *Environ. Res. Lett.* **20**, 024037 (2025).
8. Dong, T. et al. Record-breaking 2023 marine heatwaves. *Science* **389**, 369–374 (2025).
9. Hansen, J. E. et al. Global warming in the pipeline. *Oxford Open Clim. Change* **3**, kgad008 (2023).
10. Song, H., Choi, Y.-S. & Kang, H. Global change in cloud radiative effect revealed in CERES observations. *Res. Square* https://doi.org/10.21203/rs.3.rs-3781529/v1 (2023).
11. Hodnebrog, Ø. et al. Recent reductions in aerosol emissions have increased Earth's energy imbalance. *Commun. Earth Environ.* **5**, 166 (2024).
12. Kuhlbrodt, T., Swaminathan, R., Ceppi, P. & Wilder, T. A glimpse into the future: the 2023 ocean temperature and sea ice extremes in the context of longer-term climate change. *Bull. Am. Meteorol. Soc.* **105**, E474–E485 (2024).
13. Loeb, N. G. et al. Observational assessment of changes in Earth's energy imbalance since 2000. *Surv. Geophys.* **45**, 1757–1783 (2024).
14. Goessling, H. F., Rackow, T. & Jung, T. Recent global temperature surge intensified by record-low planetary albedo. *Science* **387**, 68–73 (2025).
15. Cheung, W. W. L. & Frölicher, T. L. Marine heatwaves exacerbate climate change impacts for fisheries in the northeast Pacific. *Sci. Rep.* **10**, 6678 (2020).
16. Starko, S. et al. Ecological responses to extreme climatic events: a systematic review of the 2014–2016 northeast Pacific marine heatwave. *Oceanogr. Mar. Biol. Annu. Rev.* **63**, 42–96 (2025).
17. Werb, B. E. & Rudnick, D. L. Remarkable changes in the dominant modes of north pacific sea surface temperature. *Geophys. Res. Lett.* **50**, e2022GL101078 (2023).
18. Xiao, D. & Ren, H.-L. A regime shift in North Pacific annual mean sea surface temperature in 2013/14. *Front. Earth Sci.* **10**, 987349 (2023).
19. Fuglestvedt, J. S. et al. Transport impacts on atmosphere and climate: metrics. *Atmos. Environ.* **44**, 4648–4677 (2010).
20. Yoshioka, M., Grosvenor, D. P., Booth, B. B. B., Morice, C. P. & Carslaw, K. S. Warming effects of reduced sulfur emissions from shipping. *Atmos. Chem. Phys.* **24**, 13681–13692 (2024).
21. Schmidt, G. World view. *Nature* **627**, 467 (2024).
22. Hansen, J. E. et al. Global warming has accelerated: are the United Nations and the public well-informed? *Environ. Sci. Policy Sustain. Dev.* **67**, 6–44 (2025).
23. Wood, R., Vogt, M. A. & McCoy, I. L. Aggressive aerosol mitigation policies reduce chances of keeping global warming to below 2c. *Earth's Future* **12**, e2023EF004233 (2024).
24. Ceppi, P. & Nowack, P. Observational evidence that cloud feedback amplifies global warming. *Proc. Natl. Acad. Sci. USA* **118**, e2026290118 (2021).
25. Tang, L. et al. Substantial emission reductions from chinese power plants after the introduction of ultra-low emissions standards. *Nat. Energy* **4**, 929–938 (2019).
26. Watson-Parris, D. et al. Shipping regulations lead to large reduction in cloud perturbations. *Proc. Natl. Acad. Sci. USA* **119**, e2206885119 (2022).
27. Gettelman, A. et al. Has reducing ship emissions brought forward global warming? *Geophys. Res. Lett.* **51**, e2024GL109077 (2024).
28. Gui, K. et al. A global-scale analysis of the MISR level-3 aerosol optical depth (AOD) product: comparison with multi-platform AOD data sources. *Atmos. Pollution Res.* **12**, 101238 (2021).
29. Quaas, J. et al. Robust evidence for reversal of the trend in aerosol effective climate forcing. *Atmos. Chem. Phys.* **22**, 12221–12239 (2022).
30. Twomey, S. The nuclei of natural cloud formation part ii: The supersaturation in natural clouds and the variation of cloud droplet concentration. *Geofisica pura e applicata* **43**, 243–249 (1959).
31. Albrecht, B. A. Aerosols, cloud microphysics, and fractional cloudiness. *Science* **245**, 1227–1230 (1989).
32. Shindell, D. & Faluvegi, G. Climate response to regional radiative forcing during the twentieth century. *Nat. Geosci.* **2**, 294–300 (2009).
33. von Salzen, K. et al. Clean air policies are key for successfully mitigating Arctic warming. *Commun. Earth Environ.* **3**, 222 (2022).
34. IPCC. *Climate Change 2021: The Physical Science Basis. Contribution of Working Group I to the Sixth Assessment Report of the Intergovernmental Panel on Climate Change*. https://www.ipcc.ch/report/sixth-assessment-report-working-group-i/ (2021).
35. Loeb, N. G. et al. Clouds and the Earth's radiant energy system (CERES) energy balanced and filled (EBAF) top-of-atmosphere (TOA) edition-4.0 data product. *J. Clim.* **31**, 895–918 (2018).
36. Loeb, N. G. et al. Continuity in top-of-atmosphere Earth radiation budget observations. *J. Clim.* **37**, 6093–6108 (2024).
37. Loeb, N. and Kizer, E. *Ceres Data Products*. https://ceres.larc.nasa.gov/data/ (2024).
38. Morice, C. P. et al. An updated assessment of near-surface temperature change from 1850: The HadCRUT5 data set. *J. Geophys. Res. Atmos.* **126**, e2019JD032361 (2021).
39. Morice, C. *Hadcrut5*. www.metoffice.gov.uk/hadobs/hadcrut5/ (2025).
40. Andersen, H., Cermak, J., Zipfel, L. & Myers, T. A. Attribution of observed recent decrease in low clouds over the northeastern Pacific to cloud-controlling factors. *Geophys. Res. Lett.* **49**, e2021GL096498 (2022).
41. Grosvenor, D. P. & Carslaw, K. S. Change from aerosol-driven to cloud-feedback-driven trend in short-wave radiative flux over the North Atlantic. *Atmos. Chem. Phys.* **23**, 6743–6773 (2023).
42. Raghuraman, S. P., Paynter, D., Menzel, R. & Ramaswamy, V. Forcing, cloud feedbacks, cloud masking, and internal variability in the cloud radiative effect satellite record. *J. Clim.* **36**, 4151–4167 (2023).

43. Wall, C. J. et al. Assessing effective radiative forcing from aerosol–cloud interactions over the global ocean. *Proc. Natl. Acad. Sci. USA* **119**, e2210481119 (2022).
44. Douglas, A. & L'Ecuyer, T. Quantifying cloud adjustments and the radiative forcing due to aerosol–cloud interactions in satellite observations of warm marine clouds. *Atmos. Chem. Phys.* **20**, 6225–6241 (2020).
45. Liu, Y., Koutrakis, P. & Kahn, R. Estimating fine particulate matter component concentrations and size distributions using satellite-retrieved fractional aerosol optical depth: part 1–method development. *J. Air Waste Manag. Assoc.* **57**, 1351–1359 (2007).
46. Lee, H. et al. Climatology of the aerosol optical depth by components from the multi-angle imaging spectroradiometer (MISR) and chemistry transport models. *Atmos. Chem. Phys.* **16**, 6627–6640 (2016).
47. Berrick, S. *NASA Earthdata*. https://search.earthdata.nasa.gov/ (2024).
48. Smith, S. J., Zhou, Y., Kyle, P., Wang, H. & Yu, H. A community emissions data system (ceds): emissions for CMIP6 and beyond. In *Proceedings of the 2015 International Emission Inventory Conference*. (2015).
49. Paulot, F., Paynter, D., Ginoux, P., Naik, V. & Horowitz, L. W. Changes in the aerosol direct radiative forcing from 2001 to 2015: observational constraints and regional mechanisms. *Atmos. Chem. Phys.* **18**, 13265–13281 (2018).
50. Wang, Z. et al. Incorrect asian aerosols affecting the attribution and projection of regional climate change in CMIP6 models. *NPJ Clim. Atmos. Sci.* **4**, 2 (2021).
51. O'Rourke, P. et al. *Ceds v_2021_04_21 Gidded Emissions Data*. https://data.pnnl.gov/dataset/CEDS-4-21-21 (2021).
52. Eyring, V. et al. Overview of the coupled model intercomparison project phase 6 (cmip6) experimental design and organization. *Geosci. Model Dev.* **9**, 1937–1958 (2016).
53. White, W. B., Lean, J., Cayan, D. R. & Dettinger, M. D. Response of global upper ocean temperature to changing solar irradiance. *J. Geophys. Res. Oceans* **102**, 3255–3266 (1997).
54. Cole, J. N. S. et al. The Canadian Atmospheric Model version 5 (canam5.0.3). *Geosci. Model Dev.* **16**, 5427–5448 (2023).
55. Sigmond, M. et al. Improvements in the Canadian Earth System Model (CanESM) through systematic model analysis: CanESM5. 0 and canesm5. 1. *Geosci. Model Dev.* **16**, 6553–6591 (2023).
56. von Salzen, K. Piecewise log-normal approximation of size distributions for aerosol modelling. *Atmos. Chem. Phys.* **6**, 1351–1372 (2006).
57. Wang, H. et al. Evaluation of a quasi-steady-state approximation of the cloud droplet growth equation (qdge) scheme for aerosol activation in global models using multiple aircraft data over both continental and marine environments. *Geosci. Model Dev.* **15**, 2949–2971 (2022).
58. Swart, N. C. et al. The Canadian Earth System model version 5 (CanESM5.0.3). *Geoscientific Model Development* **12**, 4823–4873 (2019).
59. Whaley, C. H. et al. Model evaluation of short-lived climate forcers for the Arctic Monitoring and Assessment Programme: a multi-species, multi-model study. *Atmos. Chem. Phys.* **22**, 5775–5828 (2022).
60. Zelinka, M. D. et al. Causes of higher climate sensitivity in CMIP6 models. *Geophys. Res. Lett.* **47**, e2019GL085782 (2020).
61. Virgin, J. G., Fletcher, C. G., Cole, J. N. S., von Salzen, K. & Mitovski, T. Cloud feedbacks from CanESM2 to CanESM5. 0 and their influence on climate sensitivity. *Geosci. Model Dev.* **14**, 5355–5372 (2021).
62. Zelinka, M. D., Klein, S. A., Qin, Y. & Myers, T. A. Evaluating climate models' cloud feedbacks against expert judgment. *J. Geophys. Res. Atmos.* **127**, e2021JD035198 (2022).
63. Lelieveld, J. et al. Effects of fossil fuel and total anthropogenic emission removal on public health and climate. *Proc. Natl. Acad. Sci. USA* **116**, 7192–7197 (2019).
64. Shindell, D. & Smith, C. J. Climate and air-quality benefits of a realistic phase-out of fossil fuels. *Nature* **573**, 408–411 (2019).
65. Bauer, S. E. et al. The turning point of the aerosol era. *Journal of Advances in Modeling Earth Systems* **14**, e2022MS003070 (2022).
66. Shindell, D. T., Faluvegi, G., Rotstayn, L. & Milly, G. Spatial patterns of radiative forcing and surface temperature response. *J. Geophys. Res. Atmos.* **120**, 5385–5403 (2015).
67. Stephens, G. L. et al. The changing nature of Earth's reflected sunlight. *Proc. R. Soc. A* **478**, 20220053 (2022).
68. Li, C. et al. Reversal of trends in global fine particulate matter air pollution. *Nat. Commun.* **14**, 5349 (2023).
69. Loeb, N. G. et al. Satellite and ocean data reveal marked increase in Earth's heating rate. *Geophys. Res. Lett.* **48**, e2021GL093047 (2021).
70. Gryspeerdt, E. et al. The impact of sampling strategy on the cloud droplet number concentration estimated from satellite data. *Atmos. Measure. Techniq.* **15**, 3875–3892 (2022).
71. Platnick, S. et al. The modis cloud optical and microphysical products: collection 6 updates and examples from terra and aqua. *IEEE Trans. Geosci. Remote Sens.* **55**, 502–525 (2016).
72. Lan, X. and Keeling, R. *Trends in Atmospheric Carbon Dioxide (CO2)*. https://gml.noaa.gov/ccgg/trends/ (2025).
73. Meinshausen, M. et al. The shared socio-economic pathway (SSP) greenhouse gas concentrations and their extensions to 2500. *Geosci. Model Dev.* **13**, 3571–3605 (2020).
74. Digby, R. A. R., von Salzen, K., Monahan, A. H., Gillett, N. P. & Li, J. The impact of uncertainty in black carbon's refractive index on simulated optical depth and radiative forcing. *EGUsphere* **2024**, 1–27 (2024).
75. Loeb, N. G. et al. New generation of climate models track recent unprecedented changes in Earth's radiation budget observed by CERES. *Geophys. Res. Lett.* **47**, e2019GL086705 (2020).
76. von Salzen, K., McFarlane, N. A. & Lazare, M. The role of shallow convection in the water and energy cycles of the atmosphere. *Clim. Dynamics* **25**, 671–688 (2005).
77. von Salzen, K. et al. The Canadian fourth-generation atmospheric global climate model (CanAM4). part i: Representation of physical processes. *Atmos. Ocean* **51**, 104–125 (2013).
78. Ackerman, A. S., Kirkpatrick, M. P., Stevens, D. E. & Toon, O. B. The impact of humidity above stratiform clouds on indirect aerosol climate forcing. *Nature* **432**, 1014–1017 (2004).
79. Mülmenstädt, J. et al. General circulation models simulate negative liquid water path–droplet number correlations, but anthropogenic aerosols still increase simulated liquid water path. *Atmos. Chem. Phys.* **24**, 7331–7345 (2024).
80. Mülmenstädt, J. et al. Can general circulation models (GCMs) represent cloud liquid water path adjustments to aerosol–cloud interactions? *Atmos. Chem. Phys.* **24**, 13633–13652 (2024).
81. Bellouin, N. et al. Bounding global aerosol radiative forcing of climate change. *Rev. Geophys.* **58**, e2019RG000660 (2020).
82. Chun, J.-Y., Wood, R., Blossey, P. & Doherty, S. J. Microphysical, macrophysical, and radiative responses of subtropical marine clouds to aerosol injections. *Atmos. Chem. Phys.* **23**, 1345–1368 (2023).
83. Kalisoras, A. et al. Decomposing the effective radiative forcing of anthropogenic aerosols based on CMIP6 Earth System Models. *Atmos. Chem. Phys.* **24**, 7837–7872 (2024).
84. Wood, R. Drizzle in stratiform boundary layer clouds. part ii: microphysical aspects. *J. Atmos. Sci.* **62**, 3034–3050 (2005).
85. Stevens, B. et al. Macv2-sp: A parameterization of anthropogenic aerosol optical properties and an associated Twomey effect for use in CMIP6. *Geosci. Model Dev.* **10**, 433–452 (2017).

86. O'Rourke, P. R. et al. Ceds v_2021_04_21 release emission data (v_2021_02_05). *Zenodo* https://doi.org/10.5281/zenodo.4737769 (2021).
87. Johansson, L., Jalkanen, J.-P. & Kukkonen, J. Global assessment of shipping emissions in 2015 on a high spatial and temporal resolution. *Atmos. Environ.* **167**, 403–415 (2017).
88. *Index of /~gwerf/GFED/GFED4*. https://www.geo.vu.nl/gwerf/GFED/GFED4/ (2023).
89. Riahi, K. et al. The shared socioeconomic pathways and their energy, land use, and greenhouse gas emissions implications: an overview. *Global Environ. change* **42**, 153–168 (2017).
90. Hoesly, R. M. et al. Historical (1750–2014) anthropogenic emissions of reactive gases and aerosols from the community emissions data system (ceds). *Geosci. Model Dev.* **11**, 369–408 (2018).
91. Painemal, D. and Zuidema, P. Assessment of MODIS cloud effective radius and optical thickness retrievals over the Southeast Pacific with VOCALS-REX in situ measurements. *J. Geophys. Res. Atmos.* https://doi.org/10.1029/2011JD016155 (2011).
92. Parsons, L. A., Brennan, M. K., Wills, R. C. J. & Proistosescu, C. Magnitudes and spatial patterns of interdecadal temperature variability in CMIP6. *Geophysical Research Letters* **47**, e2019GL086588 (2020).

Acknowledgements

We acknowledge the CERES, MODIS, MISR, and HadCRUT5 science teams for generating, maintaining, and providing observational data sets. We thank the Community Emissions Data System (CEDS), the Earth System Modelling groups, and the Earth System Grid Federation (ESGF) for the CMIP6 model data sets, and the multiple international funding agencies who support these activities. We further thank the World Climate Research Programme for coordinating and promoting CMIP6. We are grateful to Phil Rasch, Ryan Eastman, and Chris Wright for the insightful comments they provided. Support for K.v.S., S.D., and R.W. was provided by the University of Washington's Marine Cloud Brightening Research Program, which is funded by the generous support of a growing consortium of individual and foundation donors. Support for A.A., J.C., R.D., and M.S., and computing time, were provided by Environment and Climate Change Canada. S.D.'s contribution to this paper is partially funded by the Cooperative Institute for Climate, Ocean, & Ecosystem Studies (CICOES) under NOAA Cooperative Agreement NA20OAR4320271, Contribution No. 2025-1488. E.G. was supported by an Imperial College Junior Research Fellowship and a Royal Society University Research Fellowship (URF/R1/191602).

Author contributions

K.v.S. primarily designed the study and the analysis; R.D. analyzed emissions, prepared, and directed the CanAM5.1-PAM simulations; E.G. produced the MODIS cloud droplet data; J.C. and A.A. developed CanAM5.1-PAM capabilities for clouds and aerosols; L.F.-L. analyzed aerosols and climate in CanAM5.1-PAM; all authors, including S.D., M.S., and R.W., discussed the results and contributed to the writing.

Competing interests

The authors declare no competing interests.

Additional information

Supplementary information The online version contains supplementary material available at https://doi.org/10.1038/s41467-025-65127-x.

Correspondence and requests for materials should be addressed to Knut von Salzen.

Peer review information *Nature Communications* thanks the anonymous reviewers for their contribution to the peer review of this work. A peer review file is available.